Vol. , No. , Season , Pages

Journal of Analytical and Numerical Methods in Mining Engineering

Journal's home page: http://anm.yazd.ac.ir/

Research article

Experimental test and numerical simulation of the interaction between flaw and hole in coarse grain granite

Aram Ardalanzadeh[1], Seyed Davoud Mohammadi[1]*, Vahab Sarfarazi[2], Hossein Shahbazi[1]

1- Dept. of Geology, Bu-Ali Sina University, Hamedan, Iran
2- Dept. of Mining Engineering, Hamedan University of Technology Hamedan, Iran

*Corresponding author: E-mail: *d.mohammadi@basu.ac.ir*

(Received: Accepted:)
DOI:

Keywords

Rock hole
Flaw
Numerical
Rock bridge
PFC^{3D} soft wear

Abstract

The strength of a rock mass is directly affected by the presence of holes or flaws. This study investigates the effects of flaws and holes in granite rocks from the Alvand batholith in Hamedan. For this purpose, 19 rock cores were prepared with a length-to-diameter ratio (L/D) greater than 2. Holes and flaws with different arrangements and angles were created in these specimens. In some cases, a 10 mm diameter hole was added to the flawed specimens. The holes had a diameter of 10 mm, and artificial flaws with a 2 mm opening and a 20 mm length were created. The number of flaws varied from one to four, with angles of 0 or 45 degrees. It should be noted that one limitation during drilling was that holes drilled from the external surface sometimes caused the granite to fracture. After determining the physical and mineralogical properties of the specimens, uniaxial compressive strength (UCS) tests were performed. Strain was recorded using a strain gauge, and a camera was used to observe fracture propagation and crack formation. The specimens were then simulated using PFC3D software, and the laboratory results were evaluated. The results demonstrated a strong correlation between the laboratory findings and the numerical modeling. The presence of a hole alone caused a decrease in specimen strength; specifically, every 5 mm increase in hole diameter reduced the strength by approximately 15%. In specimens with 0-degree flaws, the strength was higher than in those with angled flaws due to the longer rock bridge. The lowest strength was observed in the specimen with four 0-degree flaws and a hole, which can be attributed to its short rock bridge compared to other specimens.

1. INTRODUCTION

Rock discontinuities, such as bedding planes, fissures, and weak surfaces, are prevalent in natural rock masses and significantly influence their strength and stability. Tunnel excavation in such rock masses often leads to severe problems, including excessive deformation of the surrounding rock, cracking and spalling of supporting concrete, and potentially even tunnel collapse [1-5]. Various definitions exist for the cracks that form in rocks containing flaws and holes. To better understand the cracking mechanism around an opening, Fig. 1 illustrates the crack growth process under uniaxial compression in a specimen with a circular opening [6]. Wong and Einstein [7] described seven types of systematic cracks formed in rock containing a single flaw, as shown in Fig. 2. In a subsequent article, they modified this classification for rock containing two flaws, increasing the number of crack types to nine (Fig. 3). In specimens with two non-parallel flaws, uniaxial compression tests reveal many different crack types, most of which appear as irregular, bending cracks. Various terminologies have been used in experimental and numerical studies to characterize and classify cracks emanating from pre-existing flaws [8]. Scholars often identify wing cracks and anti-wing cracks based on their propagation path morphology [9, 10]. The primary crack is typically considered a tensile wing crack [11-13], while secondary cracks are usually classified as shear cracks or mixed tensile-shear cracks. By observing the cracking mode and failure morphology of flawed specimens, the failure process under uniaxial compression can be simplified. Fig. 4 presents a simplified model of the cracking modes, which can be classified into three types: wing cracks, coplanar secondary cracks, and oblique secondary cracks [8]. The influence of weakness planes and joint orientation angles on the strength of jointed rock under uniaxial and triaxial conditions has also been investigated by other researchers. For example, Moomivand [14] studied the effects of orientation, number of sets, and frequency of discontinuities on rock strength under triaxial stress. He showed that the axial strength of a specimen with one set of discontinuities decreases slightly as the orientation angle increases from 0° to 30° under most confining pressures. Similarly, Aminpour and Moomivand [15] investigated the effect of discontinuity roughness and orientation on the parameters of rock failure criteria under triaxial compressive stress. Their results demonstrate that both the roughness and orientation angle of discontinuities significantly affect the parameters of failure criteria for jointed rock. Huang et al. [16] investigated the uniaxial compressive strength, mechanical properties, and crack propagation of sandstone containing oval-shaped holes. They concluded that as the minor diameter of the elliptical hole increases, both the crack initiation stress and the peak stress decrease linearly. With the development of computer technology, numerical methods have been widely applied in engineering rock mass research [17, 18]. For example, Li et al. [18] studied the relationship between holes and cracks in rocks under uniaxial compression using PFC^{2D} software. Their results showed that the simulations were highly consistent with experimental data. Wu et al. [19] experimentally and numerically studied the interaction between holes and fissures in rock-like materials under uniaxial compression. Their results demonstrate that the peak strength, peak strain, and elastic modulus all decrease nonlinearly as the horizontal distance between the centroids of the holes increases. Wu et al. [20] studied the mechanical and fracture behavior of brittle rocks containing two U-shaped holes under axial loading. Their stress analysis showed that concentrated stress around the openings effectively explains the fracture behavior. Tao et al. [21] investigated the dynamic response of pre-stressed hollow rocks under fast, transient loading and showed that the combination of static pre-stress and dynamic stress increases initial crack formation in the rock. Zhu and Li [22] investigated crack behavior and its stress threshold in sandstones containing square holes. By comparing two rock specimens—one with a 45-degree square hole and the other with a 0-degree square hole—under loading conditions, they concluded that a specimen with a 45-degree hole is more prone to crack propagation. Zhang et al. [23] studied the effect of the placement angle of circular holes in sandstone using laboratory tests and PFC2D software. They showed that the peak strength and stress initially decrease but then increase as the placement angle of the cracks grows. Similarly, they concluded that different cracking mechanisms ultimately alter the local stress and mechanical behavior of the specimen. Zhang et al. [24] investigated the rock fracture mechanism at different loading speeds using PFC2D software and acoustic emission monitoring. They stated that the overall process of fracture progression is not affected by the loading rate, but the stress required to reach each stage is. As the external load increases, particles in the specimen are continuously compressed, rotated, and displaced, a process accompanied by energy loss through the formation of tensile and shear cracks. Zhu et al. [25] examined stress distribution and the mechanical properties of porous granite under cyclic triaxial loading. They showed that cavity diameter significantly affects tensile cracks, the compressive-shear failure zone, and compressive stress distribution. As the hole diameter increases, the peak strength decreases, while the number of cracks and the extent of plastic deformation increase. With increasing cyclic axial stress, the elastic modulus decreases at a rate that follows a "first decrease, then increase" pattern, and Poisson's ratio also increases. In 2008, Yang et al. [26] studied the mechanism of crack growth and coalescence in cylindrical marble specimens containing two closed cracks under triaxial compression. Their research indicated that in a rock containing an inclined crack under compression, new tensile cracks initiate from the crack tip and grow perpendicularly to the main crack. In 2019, Huang et al. [27] used numerical modeling and experiments to investigate the effect of discontinuity angle, distance, and length on the uniaxial compressive strength and Young's modulus of brittle specimens. The results showed that the mechanical characteristics, fracture pattern, and compressive strength are most affected by the joint angle. Liu et al. [28] conducted studies on sandstones with discontinuous holes filled with weak materials to investigate the effects of such fillers on crack propagation in the rock mass. Chen et al. [29] experimentally and numerically investigated the behavior of granite blocks containing two side flaws and a tunnel-shaped opening. They found that the flaw inclination angle strongly affects the strength, cracking process, and stress distribution, while a slight change in the opening shape has little influence. Cracks initiate from the flaw tips and the top and bottom of the openings. Unlike the case of a circular opening, large compressive stress occurs at the arch feet of a tunnel-shaped opening, in addition to the arch waists. Hou et al. [30] investigated the crack propagation process in double-flawed granite under compression using digital image correlation and numerical simulation. Their results indicate that the failure strength of the double-flawed specimen increases with the flaw inclination angle, and the fracture morphology shifts from no propagation to splitting. In recent decades, researchers have applied theoretical, experimental, and numerical methods to study fracture initiation, propagation, and coalescence in rocks [27]. Consequently, many studies have demonstrated that the number, type (open or filled), shape, orientation, and spatial relationships of pre-existing fractures are the main factors governing the failure characteristics of specimens [31-34]. Shen [35] noted that crack coalescence in the rock bridge region between two pre-existing flaws can be caused by tensile failure, shear failure, or mixed tensile-shear failure. Zhang and Wong [36] conducted a uniaxial compression numerical simulation of a rock-like material with a single flaw and noted that microcrack initiation was almost entirely tensile. They also concluded that a microcrack band consists of a mixture of tensile and shear cracks. Cao et al. [9] identified seven types of crack coalescence in specimens containing two flaws under uniaxial compression. Zheng et al. [37] pointed out that there are four forms of rock-bridge coalescence based on microcrack initiation, coalescence, and failure evolution. Finally, it is evident that most of the cited articles do not focus on rock texture, and the behavior of coarse-grained rocks in this context has not been thoroughly investigated. Diao et al. [38] studied the mesoscopic damage and failure characteristics of through-boundary type locked rock masses under confining pressure. They showed that an increase in confining pressure leads to an increase in the locked rock mass's compressive strength and elastic modulus, while an increase in the rock bridge angle leads to a decrease in these properties. Thus, the aim of this research is to investigate the effects of flaws and holes on the failure mechanism of coarse-grained granite rocks in experimental tests and numerical simulations.

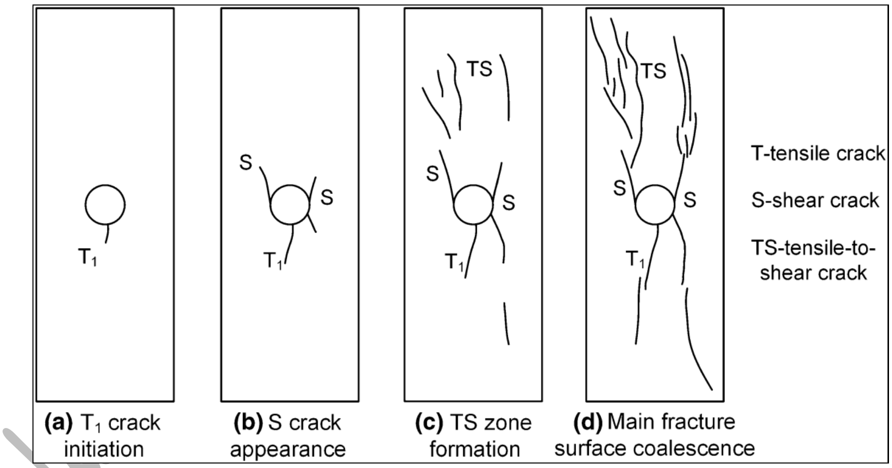

Fig. 1. Fracture evolution process of the specimen having a circular opening under monotonic compression [20]

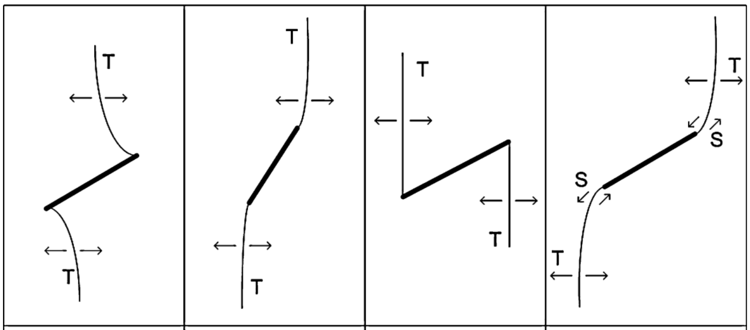

(a) Type 1 tensile crack (tensile wing crack) **(b)** Type 2 tensile crack **(c)** Type 3 tensile crack **(d)** Mixed tensile-shear crack

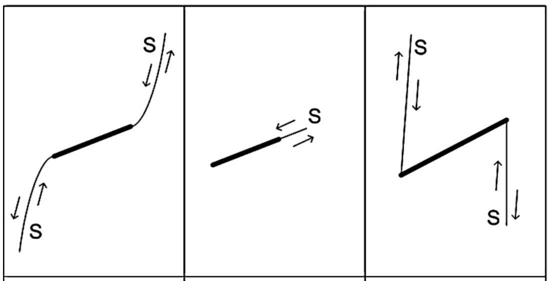

(e) Type 1 shear crack **(f)** Type 2 shear crack **(g)** Type 3 tensile crack

Fig. 2. Various crack types initiated from the pre-existing flaws. T tensile crack. S shear crack [39]

Category	Coalescence patterns	Crack types involved
1		**No** coalescence
2	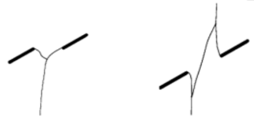 (2 cracks) (3 cracks)	**Indirect** coalescence by two or multiple cracks (crack types vary)
3		Type 2 **S** crack(s)
4	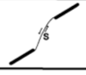	Type 1 **S** crack(s)
5	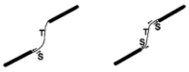	One or more type 2 **S** crack(s) and type 2 **T** crack segments between inner flaw tips
6		Type 2 **T** crack(s). There may be occasional short **S** segments present along the coalescence crack.
7		Type 1 **T** crack(s)
8		Flaw tips at the same side linked up by **T** crack(s) not displaying wing appearance (crack type not classified). There may be occasional short **S** segments present along the coalescence crack.
9		Type 3 **T** crack(s) linking right tip of the top flaw and left tip of the bottom flaw. There may be occasional short **S** segments present along the coalescence crack.

Fig.3. Crack coalescence categories. S: shear, T: tensile [39]

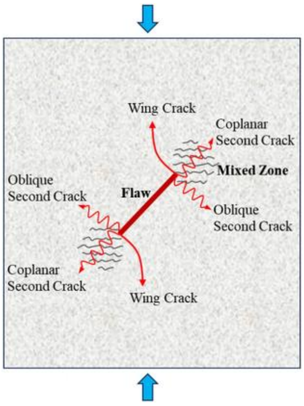

Fig. 4. Simplified cracking pattern of the cracked specimens in axial compression experiments [28]

2. GEOLOGY SETTING

The Alvand batholith is located south and west of Hamedan, in the northern part of the Sanandaj-Sirjan metamorphic zone (Fig. 5). It extends approximately 40 km in length and up to 10 km in width. The batholith is roughly oval-shaped but features a narrow central section with bulkier ends. This pluton dates to the Paleocene, with an age ranging from 64 to 70 million years [39]. The Alvand pluton is a composite body, consisting of gabbroic rocks, granites (including mylonitized varieties), and leucocratic granitoids, covering an area of approximately 800 km² [40]. Geologically, the Hamedan region forms part of the Sanandaj-Sirjan structural zone, situated at the border of the Central Iran and Zagros zones, with a general northwest-southeast trend. The origins of the granitic and gabbroic components have been studied by various researchers. Based on mineralogical, geochemical, and geological characteristics, Valizadeh and Cantagrel [41] classified the Alvand granite rocks as S-type. They identified the gabbroic section as older than the granite and, due to the presence of secondary biotites in the gabbros, proposed that the Alvand granite intruded the basic rocks of Cheshme Qasaban and North Sarkan. Conversely, Eshraghi and Mohammadi Gharai [42] attributed the intermediate rocks of Alvand to metasomatism caused by granitic fluids interacting with gabbros. The Alvand plutonic complex comprises a range of lithological units from mafic and intermediate to felsic rocks. According to some researchers, this zone is part of the Zagros orogenic belt. The lower unit of the Hamedan metamorphic complex comprises variably deformed and metamorphosed pelitic, semipelitic and psammitic metasediments as well as quartzite, amphibolite and hornblende garben schists and some calc-silicate rocks [43-44].

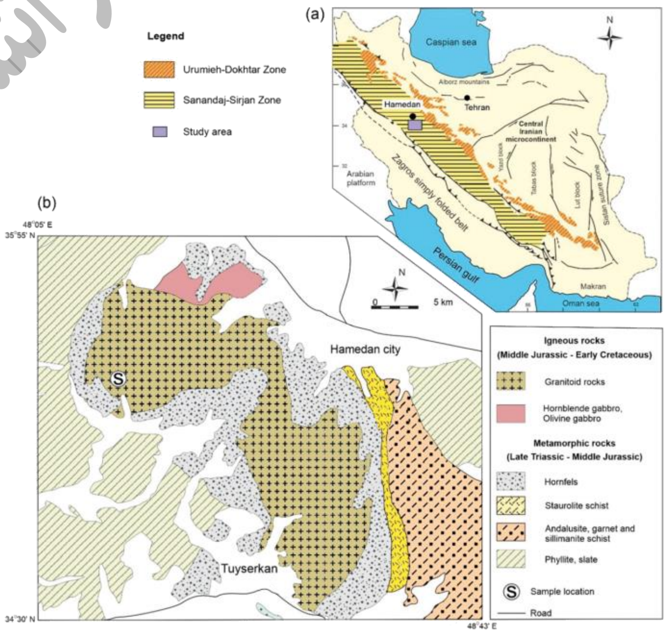

Fig. 5. Regional map of the Hamedan area [45]

3. MATERIALS AND METHODS

3.1. Sampling and preparing of core specimens

The rock blocks used in this research, with dimensions of approximately 40×40×40 cm, were collected from exposed granitic rocks of the Alvand batholith near Kahnoosh village (Coordinates: X: 249678, Y: 3844730; Fig. 6). The blocks were transported to the Engineering Geology and Geotechnics Laboratory at Bu-Ali Sina University for specimen preparation and testing. Specimens were prepared by coring to a diameter of 68 mm, ensuring a length-to-diameter ratio (L/D) greater than 2. The ends of the cores were ground to be smooth and parallel. Following the coring process, an initial guide hole was drilled into the specimens using a 5 mm diameter drill bit. This hole was then enlarged to its final diameter using a 10 mm diameter drill bit. The drilling was performed at a rotation rate of 120 RPM and a penetration rate of 5 mm/min. Subsequently, artificial flaws with a 2 mm opening and 20 mm length were created on the specimens. The number of flaws varied from one to four, with inclination angles of either 0 or 45 degrees (Fig. 7). The specifications for all specimens are provided in Fig. 8 and Table 1. Due to technical limitations, it was not possible to create fully internal flaws within the specimens. The initial experimental design called for creating edge flaws to study their effect on the failure mechanism. This configuration is also geologically relevant, as flaws in nature often terminate at a rock mass boundary. For each geometrical configuration, three identical physical specimens were prepared. However, after observing inconsistent and unexpected results from the initial tests, a fourth specimen was fabricated for these configurations to verify the findings.

Fig.6. Sampling location near Kahnoosh village

Fig. 7. Final specimens prepared rock

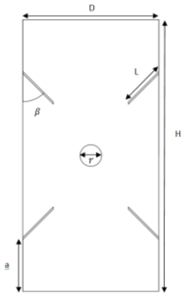

Fig. 8. Tested Granit specimens containing hole and flaw D =Width; H=Height; a=Distance flaw from the end of the specimen; L= flaw length; r= hole diameter β°= flaw angle

Table 1. Tested Granit specimens containing hole and flaw (see also fig. 13)

Specimen Shape		H(mm)	D(mm)	a(mm)	L(mm)	$\boldsymbol{\beta}$°	r(mm)
G1	Intact specimen	142	68	-	-	-	-
G2	Specimen with hole five mm	151	68	-	-	-	5
G3	Specimen with hole 10 mm	148	68	-	-	-	10
G4	Specimen with one flaw	142	68	35	20	0	-
G5	Specimen with two flaws on one side	149	68	35	20	0	-
G6	Specimen with two flaws on both sides	154	68	35	20	0	-
G7	Specimen with four flaws	150	68	35	20	0	-
G8	Specimen with one angled flaw	136	68	35	20	45	-
G9	Specimen with two angled flaws on one side	138	68	35	20	45	-
G10	Specimen with two angled flaws on both sides	153	68	35	20	45	-
G11	Specimen with four angled flaws	139	68	35	20	45	-
G12	Specimen with one hole and one flaw	152	68	35	20	0	10
G13	Specimen with one hole and two flaws on one side	139	68	35	20	0	10
G14	Specimen with one hole and two flaws on both sides	150	68	35	20	0	10
G15	Specimen with hole and 4 flaws	143	68	35	20	0	10
G16	Specimen with hole and 1 angled flaw	140	68	35	20	45	10
G17	Specimen with hole and 2 angled flaws on one side	150	68	35	20	45	10
G18	Specimen with hole and 2 angled flaws on both sides	142	68	35	20	45	10
G19	Specimen with hole and 4 angled flaws	142	68	35	20	45	10

D =Width; H=Height; a=Distance flaw from the end of the specimen*; L= flaw length; r= hole diameter β°= flaw angle*

3.2. Physical and mechanical properties of rock specimens

In order to determine the physical and mechanical properties of the specimens, UCS, specific gravity, moisture percentage, porosity tests were performed and the results obtained were averaged for three specimens as described in table 2. The cores for testing were all prepared from a single, large rock block. The mechanical properties were determined by averaging the results from three specimens for each tested configuration, in accordance with standard practice. This approach ensures that the results are representative of the homogeneous block from which they were sourced.

Table 2. Physical and mechanical properties of intact rock specimens

Rock specimen	UCS (MPa)	$\boldsymbol{\sigma_t}$ (MPa)	E (GPa)	$\boldsymbol{\gamma}$ (gr/cm^3)	$\boldsymbol{\gamma_d}$ (gr/cm^3)	$\boldsymbol{\gamma_{sat}}$ (gr/cm^3)	ω (%)	e	Gs
	36	4.27	26.5	2.50	2.50	2.52	0.23	0.01	2.50

UCS: Uniaxial compression strength, σ_t: Brazilian tensile strength, E: Young's modulus, γ:density, γ_d :Dry density, γ_{sat}: saturation density, ω: Moisture percentage, e:porosity ratio, GS: specific gravity.

3.3. Mineralogy characteristics of rock specimens

A thin section was prepared to study the mineralogical characteristics. The section was imaged and analyzed using a polarizing microscope at 4x magnification under cross-polarized light (XPL) (Fig. 9). The rock is composed of orthoclase, quartz, biotite, plagioclase, muscovite, and zircon, listed in order of decreasing abundance (Table 3).

Table 3. The percentage of minerals in the studied rocks

Rock specimen	Orthoclase (%)	Quartz (%)	Biotite (%)	Plagioclase (%)	Muscovite (%)	Zircon (%)
	40	25	15	10	5	5

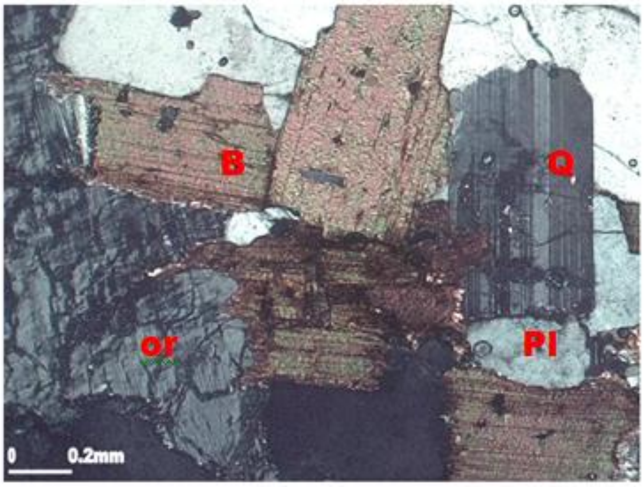

Fig 9. Microphotographs of Coarse-grained Or=Orthoclase, Q= Quartz, B= Biotite, Pl= Plagioclase

4. EXPERIMENTAL RESULTS

4.1. Strength and deformation behavior

The uniaxial compressive strength of the rock was determined using an Infra Test compression machine, with deformation recorded by a strain gauge (Fig. 10). The results of the uniaxial compressive strength tests, along with the elastic modulus for all specimens, are presented in Table 5. The intact specimen exhibited the highest strength at 36 MPa, while the specimen with two zero-degree flaws and a hole showed the lowest strength at 7.8 MPa. This is attributed to its shorter rock bridge length compared to other specimens. In specimens containing only holes, the strength decreased as the hole diameter increased. Specifically, the strength decreased by approximately 14% for the 5 mm diameter hole and by 30% for the 10 mm diameter hole. These findings indicate an inverse relationship between hole diameter and specimen strength.

For flawed specimens with similar arrangements, those with 45-degree angle flaws exhibited higher strength than those with 0-degree angle flaws. This is due to the greater distance between the flaw and the loading point, which results in a longer rock bridge. The presence of holes in the jointed specimens reduced their strength by 10-25%, which is also attributed to a reduction in rock bridge length. In the specimen with two horizontal flaws on one side, stress shielding occurred at the flaw tips. In contrast, in the specimen with a single horizontal flaw, tensile stress was concentrated at the top of the flaw without any shielding effect. Consequently, the compressive strength of the specimen with two horizontal flaws was higher than that of the specimen with one flaw. Examination of the failure in specimen G6 revealed a smooth failure surface without pulverized material, providing important evidence of tensile fracture. In specimen G10, however, shear bands with a rough surface and crushed material were observed, indicating shear cracking. Because shear cracks require more energy to initiate, specimen G10 had a higher compressive strength than specimen G6. Table 2 presents the mechanical properties of the intact rock, while Table 4 presents the properties of the flawed rock.

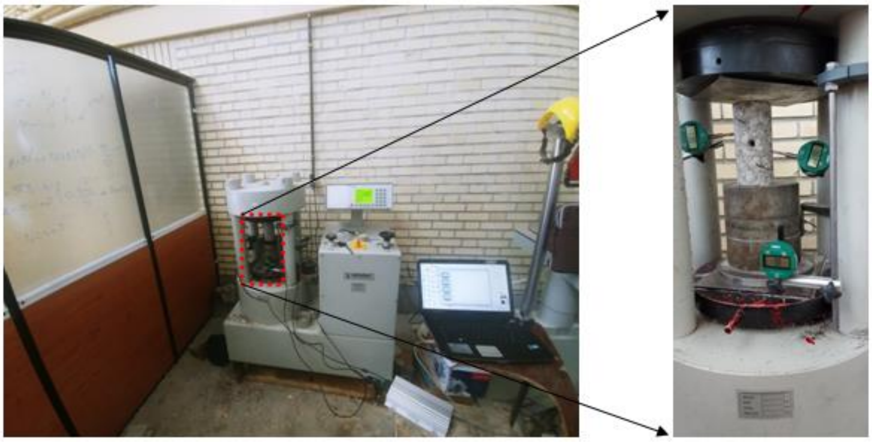

Fig. 10. Testing system (controlling laptop and Infra Test compressive strength with strain gauge)

Table 4. Test results UCS and E

Specimens	UCS_{Test}(MPa)	E (GPa)	Specimens	UCS_{Test}(MPa)	E (GPa)
G1	36	26.5	G11	15.6	20.10
G2	31.6	25.70	G12	12	20.00
G3	24.5	25.00	G13	12.5	19.70
G4	11.2	24.80	G14	7.7	18.60
G5	21	24.00	G15	7.8	13.50
G6	8	19.60	G16	20	22.00
G7	11.6	15.30	G17	18.2	20.60
G8	23.6	22.80	G18	15.5	19.30
G9	24.7	24.50	G19	13.5	19.00
G10	17.1	22.10	-	-	-

4.2. Cracking process in laboratory test

Macroscopic cracks form through the initiation, propagation, and coalescence of microcracks. Consequently, their formation is not an abrupt event but a cumulative damage process. In previous studies, scholars have used high-resolution cameras and digital image correlation (DIC) techniques to record detailed geometric representations of crack evolution [38]. These methods can identify the initiation sequence and patterns of macroscopic cracks. Specifically, DIC can precisely analyze displacement and strain fields during cracking, enabling both qualitative and quantitative analysis of the fracture process [30]. In alignment with previous research on pre-flawed or pre-holed rock materials [14, 46-47], the cracks in this study are identified as tensile cracks based on their smooth, polished surfaces and the absence of pulverized material. Previous studies indicate that crack initiation during uniaxial loading typically occurs at flaw tips or other specific locations around openings where stress is concentrated [33, 49]. This phenomenon was observed in all specimens except for the intact specimen and the specimen with a 5 mm diameter hole. The absence of stress concentration in these two cases is likely due to the large distance from the loading points and the small size of the hole relative to the specimen diameter. Analysis of the fracture videos confirms that cracking consistently initiates at the flaw tips or around the holes and propagates to the specimen's end, leading to final failure (Fig. 11).

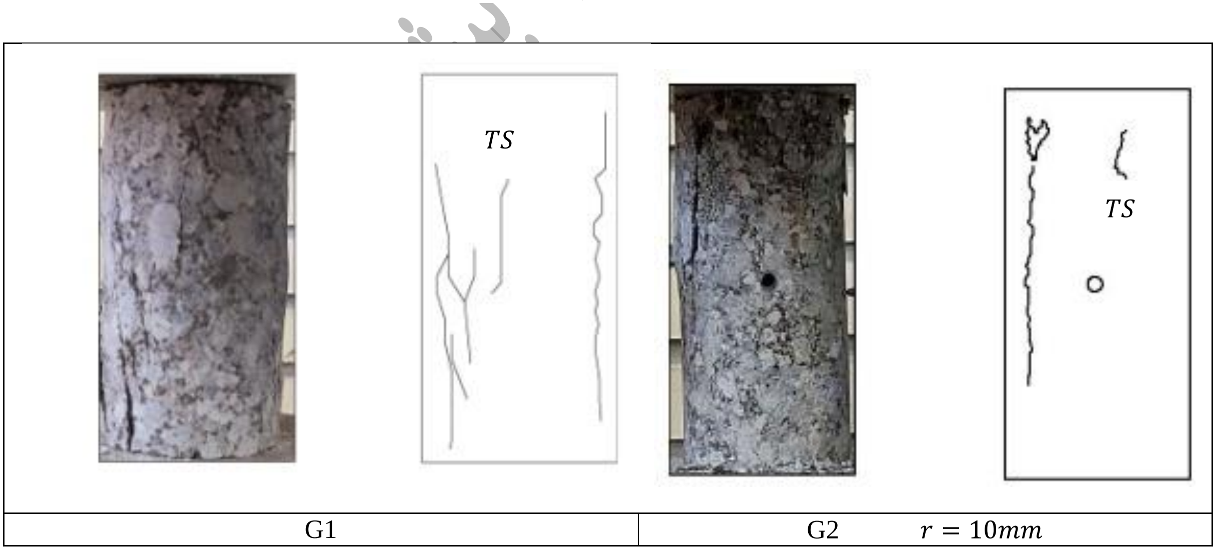

G1

G2 $r = 10mm$

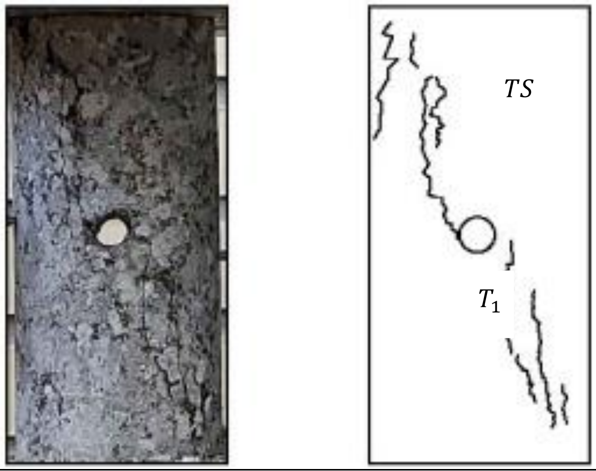	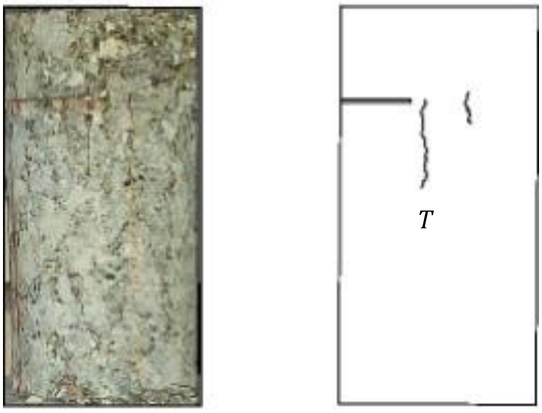
G3 $r = 10mm$	G4 $\beta = 0°$
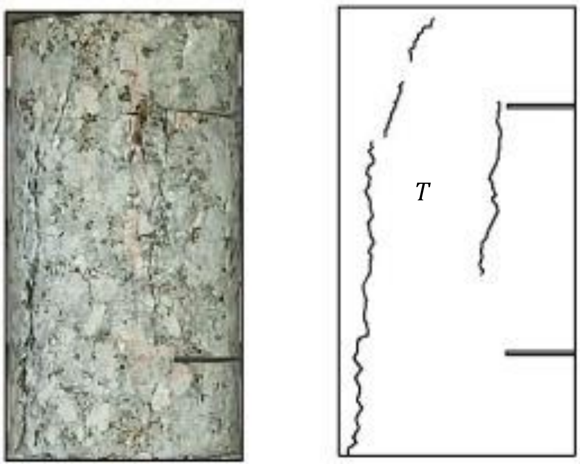	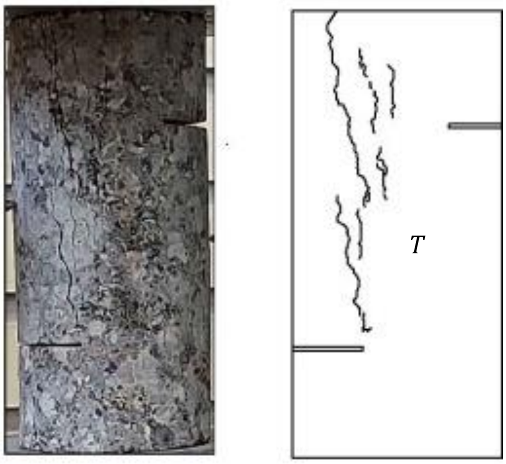
G5 $\beta = 0°$	G6 $\beta = 0°$
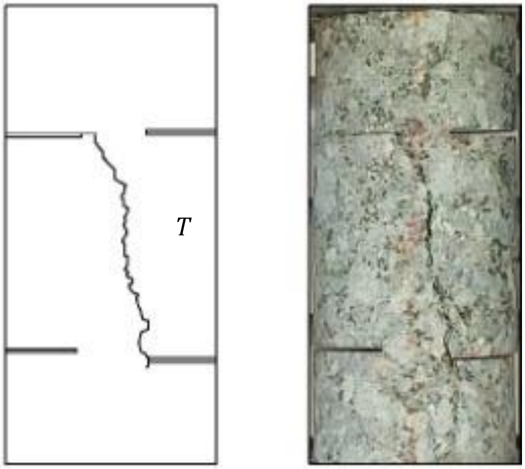	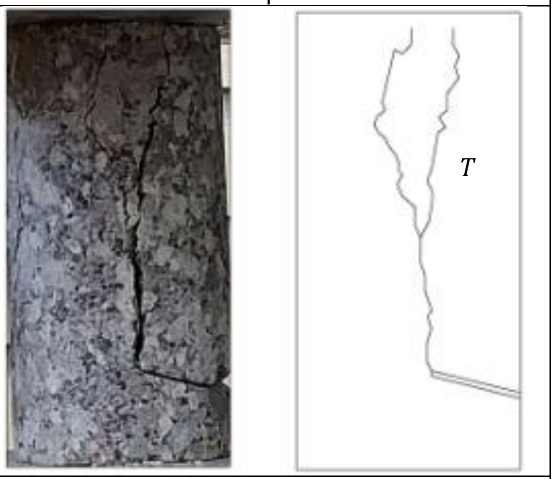
G7 $\beta = 0°$	G8 $\beta = 45°$

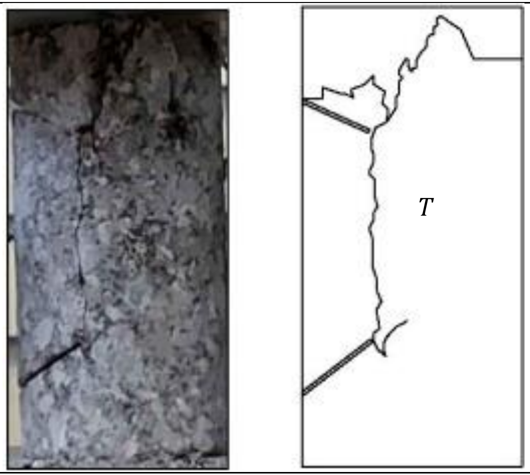	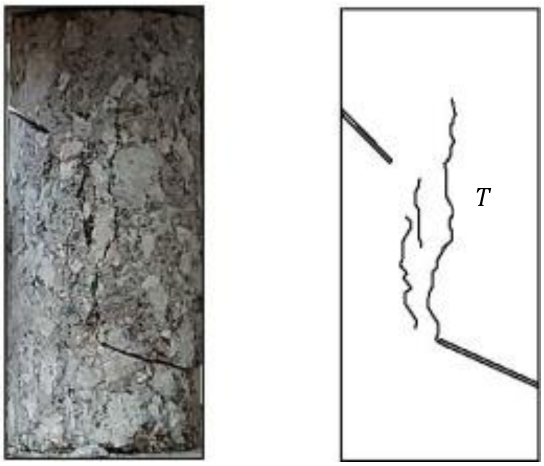
G9 $\beta = 45^\circ$	G10 $\beta = 45^\circ$
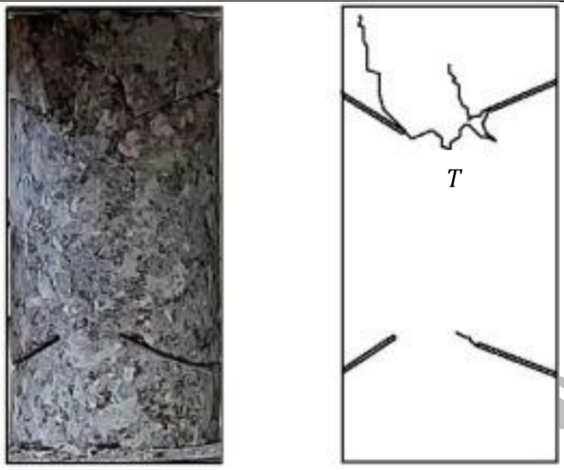	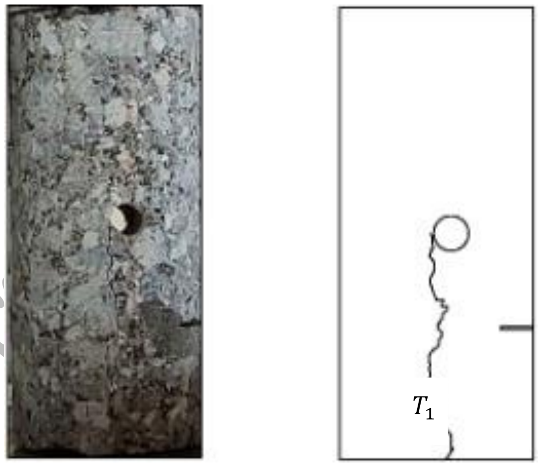
G11 $\beta = 45^\circ$	G12 $\beta = 0^\circ$ $r = 10mm$
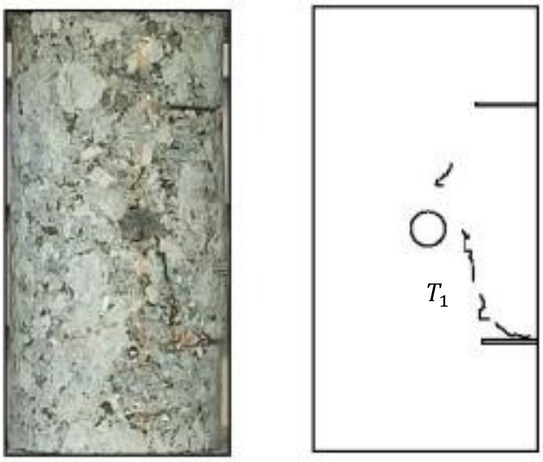	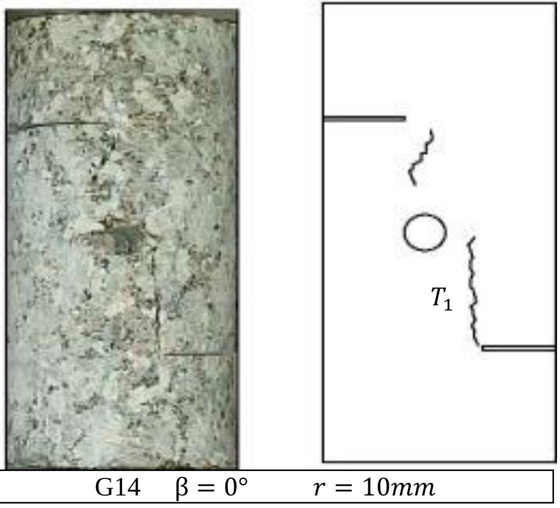
G13 $\beta = 0^\circ$ $r = 10mm$	G14 $\beta = 0^\circ$ $r = 10mm$

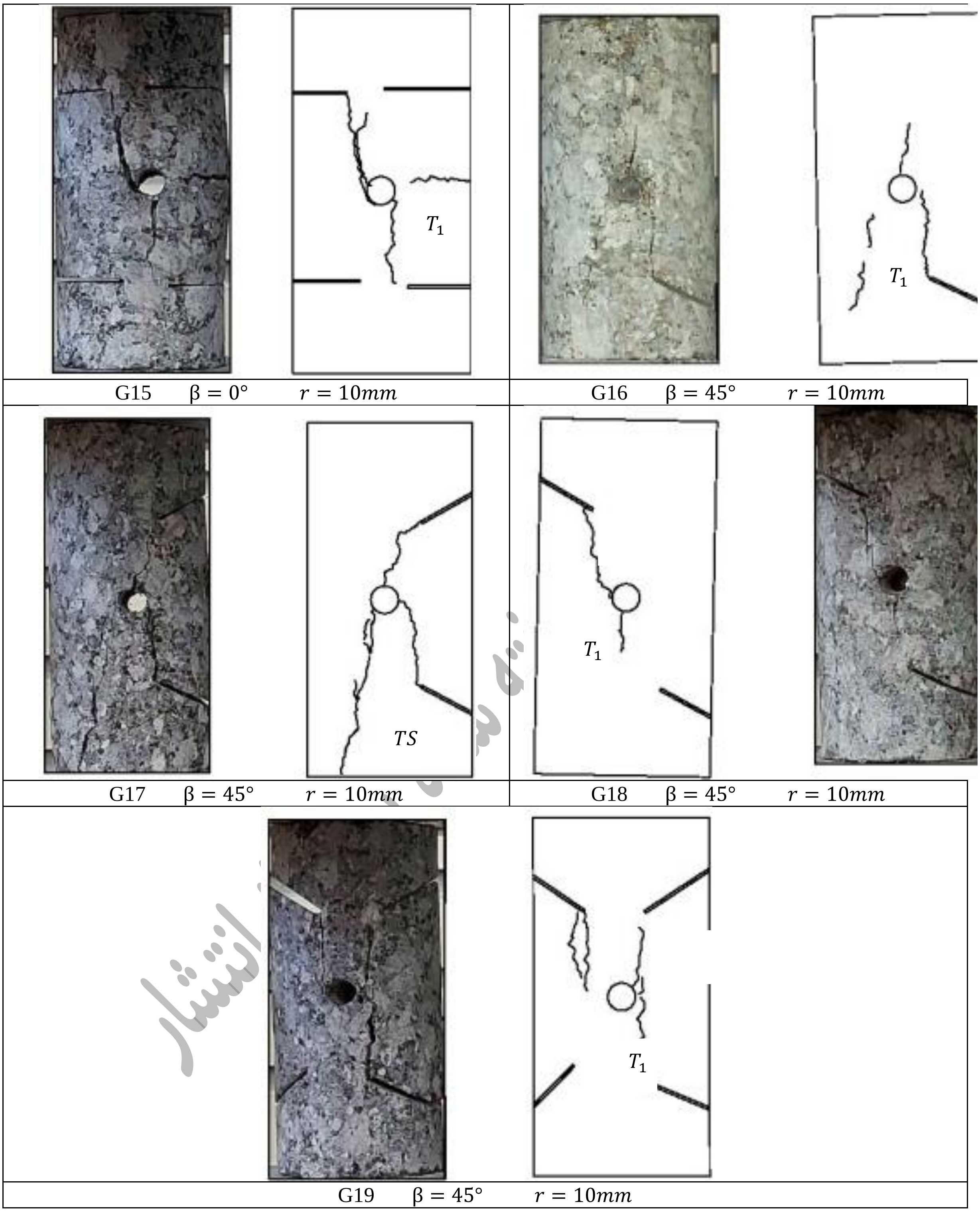

G15 $\beta = 0°$ $r = 10mm$

G16 $\beta = 45°$ $r = 10mm$

G17 $\beta = 45°$ $r = 10mm$

G18 $\beta = 45°$ $r = 10mm$

G19 $\beta = 45°$ $r = 10mm$

Fig. 11. Ultimate failure modes with different flaw angles in laboratory test, r= hole diameter, β= flaw angle, S=shear crack, T=tensile crack, TS= tensile- to- shear crack.

5. NUMERICAL MODELING

5.1. Model setup and micro-parameters calibration

The Particle Flow Code (PFC) software provides distinct two-dimensional (2D) and three-dimensional (3D) modeling environments. It employs the Discrete Element Method (DEM), representing materials as assemblies of discrete particles—disks in 2D and spheres in 3D. This approach allows the software to model complex solid mechanics problems and the quasi-static or dynamic flow of particulate materials. PFC^{2D}, the 2D variant, utilizes a powerful logic for simulating the mechanical behavior of geomaterials.

The spheres were bonded together using a flat-joint contact model. The interactions between these contacts followed a Mohr-Coulomb failure criterion. A tensile crack was generated when the tensile force exceeded the contact's tensile strength. Similarly, a shear crack was generated when the shear stress exceeded the cohesion value. Table 5 presents the micro-parameters used for the particles and the flat-joint contacts. The particle micro-parameters include the minimum radius, maximum radius, density, and Young's modulus. The flat-joint micro-parameters include tensile strength, cohesion, the ratio of normal to shear stiffness, and the Young's modulus of the bond itself. The macro parameters of Poisson's ratio were calibrated by adjusting the ratio of normal to shear stiffness of the flat-joint contacts. Similarly, the macro parameters of Young's modulus were calibrated using the Young's modulus micro-parameter. The uniaxial compressive strength (UCS) and Brazilian tensile strength (BTS) were calibrated against the cohesion and tensile strength micro-parameters, respectively.

The numerical model was calibrated using data from uniaxial compressive and Brazilian tensile tests. The micro-parameters—including tensile strength, cohesion, Young's modulus, stiffness ratio, friction angle, and density—were iteratively adjusted until the model's mechanical response matched the laboratory results. For this calibration, a cylindrical specimen with a diameter of 54 mm and a height of 108 mm, comprising 49,034 particles, was initially created. The input parameters, listed in the table 5, were assigned to the model. Once calibrated, the model dimensions were scaled to the actual laboratory specimen size (68 mm diameter and 136 mm height, based on an L/D ratio >2). This final model was then used to simulate the various flaw and hole configurations tested in the laboratory. After constructing the intact model in PFC^{3D}, flaws and holes were introduced to simulate their behavior under compression. Several methods can simulate these discontinuities, such as reducing the bond strength of particles in the flaw region, using smooth-joint contact models, or deleting particles at specific locations [8].

In this research, non-persistent (non-closed) flaws were simulated by deleting particles at specific locations. The flaws had a fixed length of 20 mm and an opening of 2 mm, with inclination angles of 0 or 45 degrees. The holes had diameters of 5 mm and 10 mm and were located at the center of the specimen (Fig. 12).

Figure 13 illustrates the different configurations of holes and flaws that were modeled.

Table.5. The micro-parameters used in the PFC^{3D} model for Granite

Micro-parameter	Value	Micro-parameter	Value
Minimum radius, R_{min} (mm)	0.009	Young's modulus of the Flat joint, Ec' (GPa)	13.5
Maximum radius, R_{max} (mm)	0.012	Ratio of normal to shear stiffness of the Flat joint	1.6
Density, (kg/m3)	2500	Flat joint cohesion, c' (MPa)	11
Flat joint-bond tensile	4.3	Young's modulus of the particle, Ec (GPa)	27

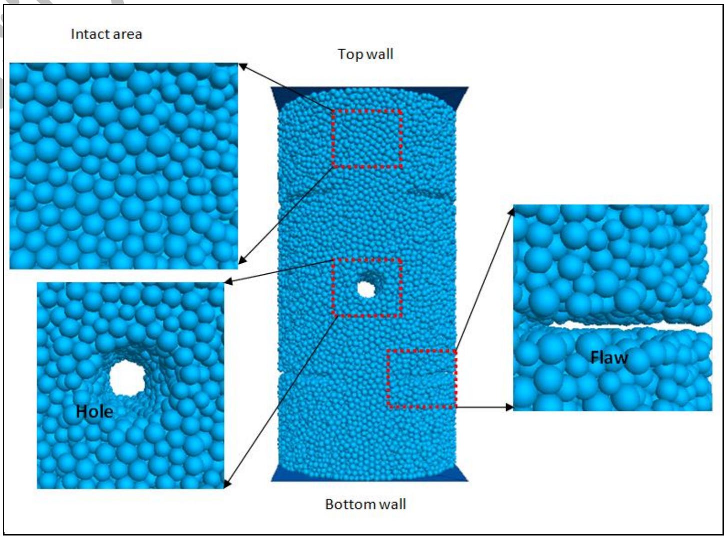

Fig.12. The established numerical specimens using PFC^{3D}

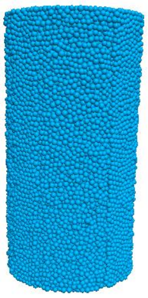	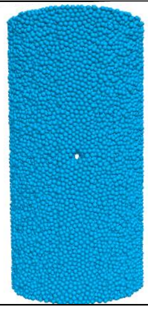	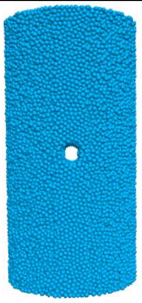	
G1 Intact model	G2 Model with a 5 mm diameter hole	G3 Model with a 10 mm diameter hole	G4 Model with one flaw
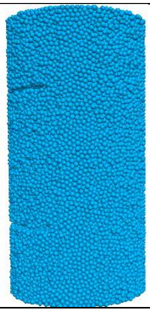	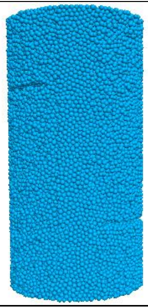	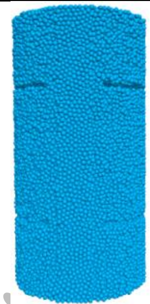	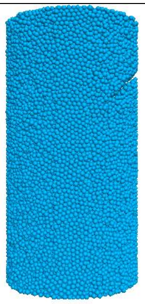
G5 Model with two horizontal flaws on one side	G6 Model with two horizontal flaws on both sides	G7 Model with four horizontal flaws on both sides	G8 Model with one diagonal (45°) flaw
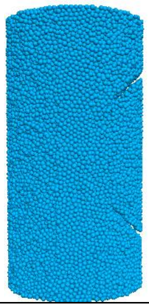	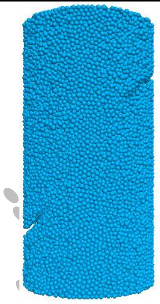	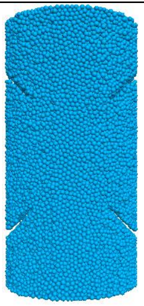	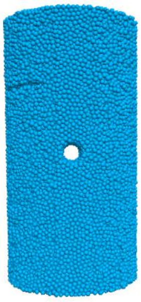
G9 Model with two diagonal flaws on one side	G10 Model with two diagonal flaws on both sides	G11 Model with four diagonal flaws	G12 Model with one hole and one flaw
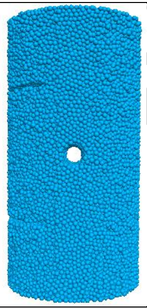	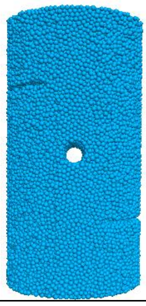	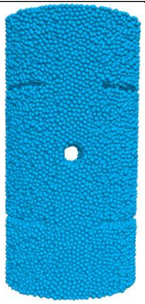	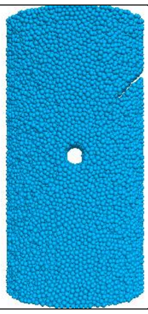
G13 Model with one hole and two horizontal flaws on one side	G14 Model with one hole and two horizontal flaws on both sides	G15 Model with one hole and four horizontal flaws	G16 Model with one hole and one diagonal flaw

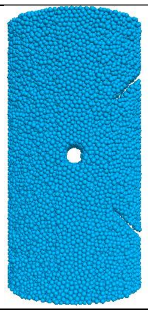	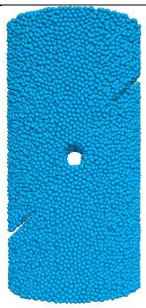	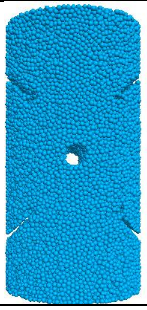	
G17 Model with one hole and two diagonal flaws on one side	G18 Model with one hole and two diagonal flaws on both sides	G19 Model with one hole and four diagonal flaws	

Fig. 13. Final specimens prepared in numerical modelling before loading.

5.2. Strength and deformation behavior

The results of the numerical modeling are presented in Table 6. The difference between the laboratory and numerical results for compressive strength ranges from 1% to 15%. The numerical model consistently predicts higher strength values, which can be attributed to the presence of inherent microcracks and imperfections in the physical rock specimens that are not fully captured in the simulation. Despite this discrepancy, the overall results demonstrate a strong correlation between the numerical models and the laboratory tests. This validates the accurate selection of input parameters for the models. Furthermore, the Young's modulus values show a maximum difference of only 4%, indicating that the models very accurately replicate the specimens' deformational behavior during the elastic loading stage.

Table 6. UCS and E parameters obtained from numerical modelling

Specimens	UCS$_{Test}$(MPa)	E (GPa)	Specimens	UCS$_{Test}$(MPa)	E (GPa)
G1	37	27	G11	16.6	20.42
G2	32	26.00	G12	13	20.09
G3	25.6	25.20	G13	13.8	19.75
G4	12.5	25.00	G14	8.69	18.80
G5	22	24.10	G15	8.8	14.00
G6	9.24	20.00	G16	20.8	22.11
G7	12	15.49	G17	19.2	20.87
G8	24.8	22.96	G18	16.5	19.80
G9	26	24.90	G19	14.7	19.34
G10	18	22.50	-	-	-

5.3. Cracking process in numerical modelling

Fig. 14 shows the ultimate failure modes of the specimens and the positions of the created tensile cracks. These results validate the numerical model's feasibility and confirm the accuracy of the micro-parameters used in PFC.

	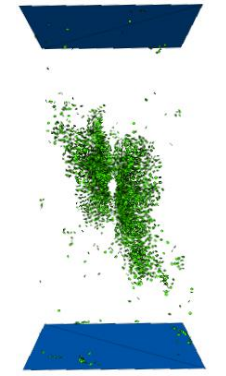
G1	G2 $r = 10mm$
	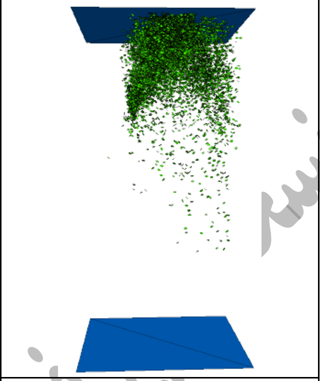
G3 $r = 10mm$	G4 $\beta = 0^\circ$
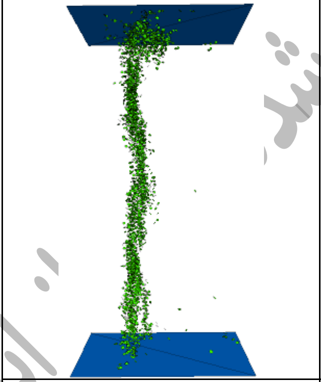	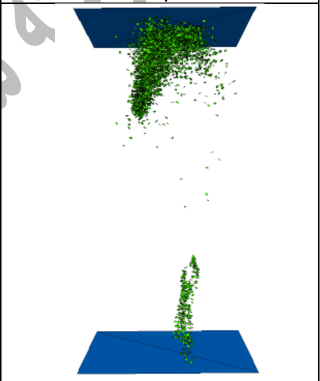
G5 $\beta = 0^\circ$	G6 $\beta = 0^\circ$
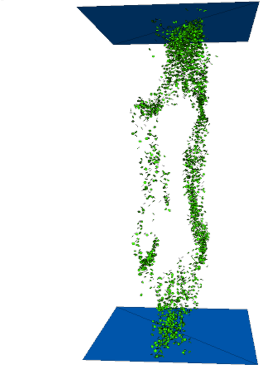	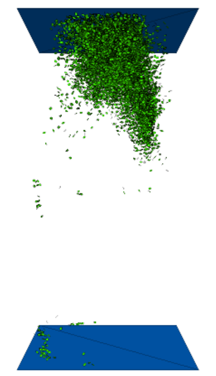
G7 $\beta = 0^\circ$	G8 $\beta = 45^\circ$

	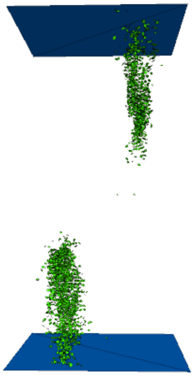
G9 $\beta = 45^\circ$	G10 $\beta = 45^\circ$
	
G11 $\beta = 45^\circ$	G12 $\beta = 0^\circ \quad r = 10mm$
	
G13 $\beta = 0^\circ \quad r = 10mm$	G14 $\beta = 0^\circ \quad r = 10mm$
	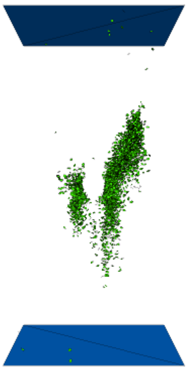
G15 $\beta = 0^\circ \quad r = 10mm$	G16 $\beta = 45^\circ \quad r = 10mm$

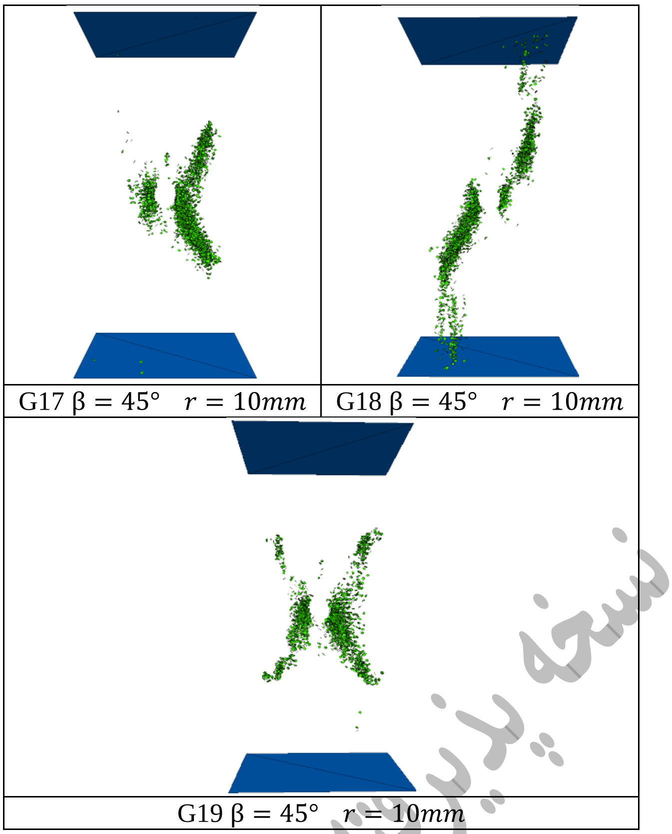

G17 β = 45° $r = 10mm$

G18 β = 45° $r = 10mm$

G19 β = 45° $r = 10mm$

Fig.14. Failure modes in numerical simulation , r= hole diameter, β= flaw angle

6. THE RESULTS OF UNIAXIAL COMPRESSIVE STRENGTH AND MODULUS OF ELASTICITY

The results of uniaxial compressive strength and modulus of elasticity obtained from the laboratory and numerical simulation are presented in Fig 15 and 16. The strengths obtained from the numerical method show more values than the laboratory ones. Moreover, the values of the modulus of elasticity obtained from the numerical method are slightly higher than the values obtained from the laboratory Test.

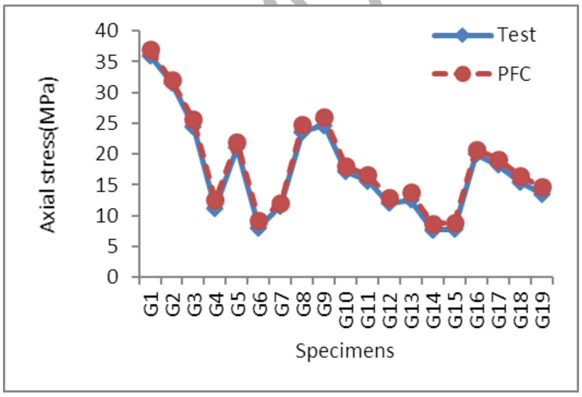

Fig.15. Comparison of axial stress in laboratory tests and numerical simulation

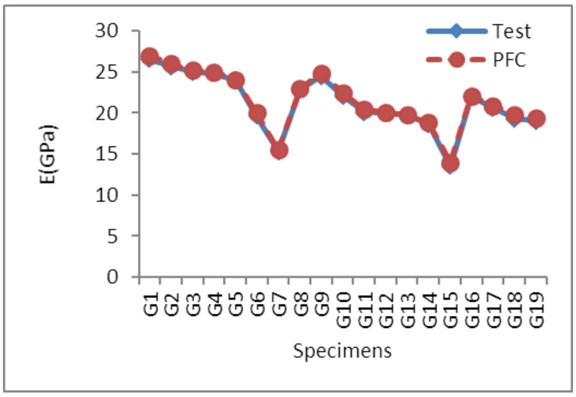

Fig.16. Comparison of elastic modulus in laboratory tests and numerical simulation

The mechanical behavior of the specimens during testing was broadly similar; therefore, the stress-strain diagrams for only two representative specimens, G1 and G7, are presented for detailed evaluation. Figures 17 and 18 compare the stress-strain curves from the laboratory tests and numerical simulations. It can be seen that the curves obtained from the PFC model are in good agreement with the experimental results for both specimens. Key features of the mechanical response, such as the elastic deformation stage, stress drops, and fluctuations caused by crack initiation, are all proficiently reproduced by the numerical model.

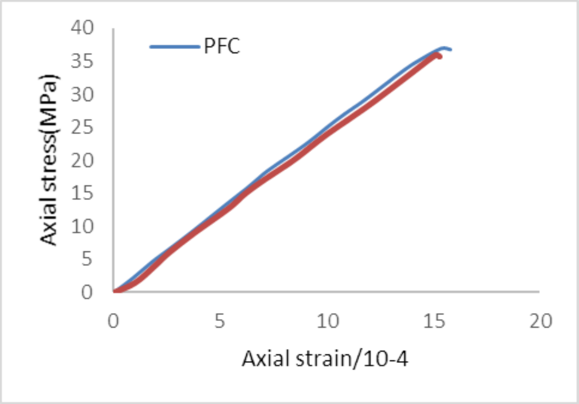

Fig.17.Comparison of stress-strain curves from laboratory tests and numerical simulations in specimen G1

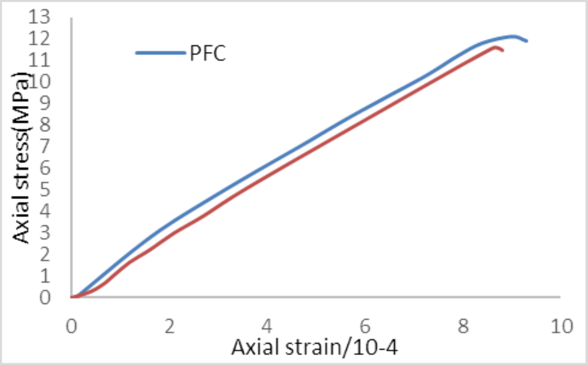

Fig.18. Comparison of stress-strain curves from laboratory tests and numerical simulations in specimen G7

7. DISCUSSION

The failure mechanisms observed in the numerical models are summarized below, categorized by flaw and hole configuration.

A. Models with holes only:

-Five mm diameter hole: Limited shear bands developed on both sides of the hole. A dominant tensile crack then propagated through the specimen, causing failure.

-Ten mm diameter hole: More extensive shear bands developed on both sides of the hole compared to the 5 mm model. Similarly, a major tensile crack propagated through the specimen, leading to failure.

B. Models with flaws only:

- Horizontal flaws: Cracking was primarily tensile. In configurations with multiple flaws, cracks initiated from the flaw tips and typically coalesced with each other or with the specimen boundary. In the case of four flaws, cracks propagated parallel to the loading axis to achieve coalescence.
- Diagonal (oriented) flaws: The failure pattern was similar to that of horizontal flaws, dominated by tensile cracks that initiated at the flaw tips and coalesced diagonally or, in the case of multiple flaws, parallel to the loading axis.

C. Models with combined flaws and a central hole:

- The presence of a hole introduced shear bands around its periphery in all combined models.
- The tensile cracking behavior from the flaws was similar to that described in section B, with cracks propagating from the flaw tips until coalescence.
- A key observation is that the presence of the hole concentrated damage, reducing the overall damage area compared to models with only flaws.

D. Key conclusions from comparisons:

-The damage intensity was higher in models containing only flaws compared to those containing both flaws and a hole.

-In models containing flaws and a hole, the total damage area decreased as the number of flaws increased.

-In models containing oriented (diagonal) flaws and a hole, the damage area decreased as the flaw angle increased.

-A direct comparison between Fig. 11 (physical samples) and Fig. 14 (numerical models) confirms that the numerical simulation successfully replicated the same failure patterns observed in the laboratory.

8. CONCLUSIONS

This study investigates the effects of flaws and holes on the fracture mechanism of coarse-grained granite using integrated experimental and numerical simulations. Non-persistent flaws with a length of 20 mm, an opening of 2 mm, and angles of 0 or 45 degrees were simulated in the Particle Flow Code (PFC) software by deleting particles at specific locations. Circular holes with diameters of 5 mm and 10 mm were positioned at the center of the specimens. A comprehensive series of models, including intact, pre-holed, pre-flawed, and combined flaw-hole configurations, were subjected to uniaxial compression tests. The key findings are as follows:

1. Newborn tensile crack was initiated from flaw tips regardless of pre-hole hole. Shear cracks were developed at the left and right side of the hole.
2. Tensile crack is smooth and slickenside while shear crack is wavy with pulverized material.
3. The highest strength was related to the intact specimen, followed by the specimen with a hole diameter of 5 mm. The lowest strength was related to the specimen with four horizontal flaws and a hole with a diameter of 10 mm.

4. Specimens solely having holes showed that the strength of the specimen decreased with the increase in the hole diameter; in the 5 mm diameter hole specimen, it decreased by about 14%, and in the specimen with a 10 mm diameter hole, it decreased by about 30%. This indicates a direct relationship between the increase in the diameter of the hole and the decrease in the strength of the specimen.
5. Specimen solely having one flaw with a hole, due to the large distance between the flaw and the hole, the presence of the hole did not have much effect on the strength of the specimen.
6. Flaws having a 45-degree angle of x have higher strength than flaws with a 0-degree angle in the same arrangement, which can be due to the greater distance between the end of the flaw and the loading edges.
7. In the 0-degree angle flaws specimens under the same conditions, the presence of holes reduced the strength by a maximum of 10%, which is due to the shortening of the fracture bridge.
8. Flaws having a 45-degree angle under the same conditions, the presence of holes reduced it by a maximum of 25%, which is due to the shortening of the fracture bridge.
9. Experimental test results are in a good accordance with numerical simulation.
10. The results of this research help engineers to have a close view on the response of rock mass containing rock joint and rock hole (cavity) under uniaxial compression.

Acknowledgements

This work was supported by the president research office of Bu-Ali Sina University, Hamedan, Iran (grant numbers 1400.07), which is gratefully acknowledged. Also preparation of rock specimens and conducting experiments was undertaken in the Engineering Geology and Geotechnics Laboratory of Bu-Ali Sina University. Therefore, deepest appreciation to all the contributions made in this field.

Conflict of Interest

The authors declare that they have no conflict of interest.

REFERENCES

[1] Gong, Q. Yin, L. Wu, S. Zhao, J. Y, Ting. (2012). Rock burst and slabbing failure and its influence on TBM excavation at headrace tunnels in Jinping II hydropower station, Engineering Geology, 124(1). https://doi.org/10.1016/j.enggeo.2011.10.007.

[2] Jia, P. Tang, C. (2008). Numerical study on failure mechanism of tunnel in ed rock mass, Tunnelling and Underground Space Technology, 23. https://doi.org/10.1016/j.tust.2007.09.001.

[3] Huang, F., Zhu, H., Xu, Q., Cai, Y., Zhuang, X.2013. The effect of weak interlayer on the failure pattern of rock mass around tunnel—scaled model tests and numerical analysis, Tunnelling and Underground Space Technology, 35. 207–218. http://dx.doi.org/10.1016/j.tust.2012.06.014.

[4] Song, J. Lee, C. Seto, M. (2001). Stability analysis of rock blocks around a tunnel using a statistical modeling technique, Tunnelling and Underground Space Technology 16(4). http://dx.doi.org/10.5897/IJPS11.777.

[5] Lai, H. Zhang, J. Zhang, L. Chen, R.Yang, W. (2019). A new method based on centrifuge model test for evaluating ground settlement induced by tunneling, KSCE Journal of Civil Engineering, 23 (6). http://dx.doi.org/10.1007/s12205-019-0780-0.

[6] Carter, B. Lajtai, E. Petukhov, A. (1991). Primary and remote fracture around underground cavities. International Journal for Numerical and Analytical Methods in Geomechanics, 15. doi:10.1002/nag.1610150103.

[7] Wong, L. Einstein, H. 2009. Systematic evaluation of cracking behavior in specimens containing single flaws under uniaxial compression, International Journal of Rock Mechanics and Mining Sciences, 46. http://dx.doi.org/10.1016/j.ijrmms.2008.03.006.

[8] Qi, J. Zhou, L. Zhang, H. Chen, J. Ma, L. Shi, T. (2023). Research on crack evolution law and mechanical analysis of three cracked rock masses subjected to compression load. Theoretical and Applied Fracture Mechanics. 127. https://doi.org/10.1016/j.tafmec.2023.104035.

[9] Cao, P. Liu, T. Y. Pu, C. Z. and Lin, H. (2014). Crack propagation and coalescence of brittle rock-like specimens with pre-existing cracks in compression. Engineering Geology, 187. http://dx.doi.org/10.1016/j.enggeo.2014.12.010.

[10] Cheng, H. Zhou, X. Zhu, J. Qian, Q. (2016). The effects of crack openings on crack initiation, propagation and coalescence behavior in rock-like materials under uniaxial compression. Rock Mechanics and Rock Engineering, 49(9), https://link.springer.com/article/10.1007/s00603-016-0998-9.

[11] Yang, S. Yang, D. Jing, H. Li, Y. Wang, S. (2012).An experimental study of the fracture coalescence behaviour of brittle sandstone specimens containing three fissures. Rock Mechanic and Rock Engineering, 45(4). http://dx.doi.org/10.1007/s00603-011-0206-x.

[12] Weng, L. Li, X. Taheri, A. Wu, Q. Xie, X. (2018). Fracture evolution around a cavity in brittle rock under uniaxial compression and coupled static–dynamic loads. Rock Mechanic and Rock Engineering, 51. https://doi.org/10.1007/s00603-017-1343-7.

[13] Zhang, X. Liu, Q. Wu, S. Tang, X. H. (2015). Crack coalescence between two non-parallel flaws in rock-like material under uniaxial compression. Engineering Geology 199. https://doi.org/10.1016/j.enggeo.2015.10.007.

[14] Moomivand, Hassan. (2013). Effects of orientation, frequency, and number of sets of discontinuities on rock strength under triaxial stresses. Arabian Journal of Geosciences. 7. https://doi.org/10.1007/s12517-013-1069-0

[15] Aminpour, F. & Moomivand, H. (2019). Effect of discontinuity roughness and orientation on the parameters of the rock failure criterion under triaxial compressive stress. Journal of the Southern African Institute of Mining and Metallurgy. 119. 1047-1060. https://doi.org/10.17159/2411-9717/113/324/19/2019.

[16] Huang, Y. Yang, Sh. Hall, M, R. Tian, W. Yin, P. (2018). Experimental study on uniaxial mechanical properties and crack propagation in sandstone containing a single oval cavity. Archives of Civil and Mechanical Engineering, 18. https://doi.org/10.1016/j.acme.2018.04.005.

[17] Guo, Y,Q, Huang D, Cen DF. (2024). Crack propagation and coalescence mechanism of a rock bridge between a parallel fissure pair in a direct shear test with unloading normal stress. International journal of geomechanics. 24(1):04023258. doi: 10.1061/IJGNAI.GMENG-7626.

[18] Li, KP. Li, Y. Yin, FT. Dai, F. Wang, C. Zhang, SW. Wang, K. (2024). Mechanical properties and failure mechanism of rock-like specimens with arc-shaped flaws under freeze–thaw cycles. Theoretical and Applied Fracture Mechanics 130(1-2). https://doi.org/10.1016/j.tafmec.2024.104275.

[19] Wu, T. Gao, . Zhou, Y. Li, Jianwang. (2020). Experimental and numerical study on the interaction between holes and fissures in rock-like materials under uniaxial compression. Theoretical and Applied Fracture Mechanics. V 106. P 102488. https://doi.org/10.1016/j.tafmec.2020.102488.

[20] Wu, H. Zhao, G. Liang, W. (2019). Mechanical response and fracture behavior of brittle rocks containing two inverted u-shaped holes under uniaxial loading. Applied Sciences, 9. https://dx.doi.org/10.3390/app9245327.

[21] Tao, M. Ma, A. Cao, W. Li, X. Gong, F. (2017), Dynamic response of pre-stressed rock with a circular cavity subject to transient loading. International Journal of Rock Mechanics and Mining Sciences, 99. http://dx.doi.org/10.1016/j.ijrmms.2017.09.003.

[22] Zhu, Q. Li, D. (2020). Experimental investigation on crack behavior and stress thresholds of sandstone containing a square inclusion under uniaxial compression. Applied Sciences, 10. https://dx.doi.org/10.3390/app10217621.

[23] Zhang, Y. Jiang, Y. Tang, X. Chen, M. Shi, X. (2020), Cracking behavior and local stress characteristics around the opening surrounded by two intermittent: experiment and numerical simulation. Comptes Rendus Mécanique, 348(1). https://doi.org/10.5802/crmeca.4.

[24] Zhang, Y. Wang, G. Jiang, Y. Wang, Sh. Zhao, H. Jing, W. (2017). Acoustic emission characteristics and failure mechanism of fractured rock under different loading rates, Shock and Vibration, 2017(5). https://doi.org/10.1155/2017/5387459.

[25] Zhu, W. Liu, J. Tang, C. Zhao, X. Brady, B. (2005). Simulation of progressive fracturing processes around underground excavations under biaxial compression. Tunnelling and Underground Space Technology incorporating Trenchless Technology Research. http://dx.doi.org/10.1016/j.tust.2004.08.008.

[26] Yang, Sh. Jiang, Y. Xu, W. Chen, X. (2008). Experimental investigation on strength and failure behavior of pre-cracked marble under conventional triaxial compression. International Journal of Solids and Structures, 45(17). https://doi.org/10.1016/j.ijsolstr.2008.04.023.

[27] Huang, C. Yang, W. Duan, K. Fang, L. Wang, L. Bo, C. (2019). Mechanical behaviors of the brittle rock-like specimens with multi-non-persistent under uniaxial compression. Construction and Building Materials, 220. https://doi.org/10.1016/j.conbuildmat.2019.05.159.

[28] Liu, X. Zhang, K. Liu, W. Xie, J. (2022). Influence of weak inclusions on the cracking behavior of a ed rock mass containing an opening: insights from DIC-based approaches. Archives of Civil and Mechanical Engineering, 22(4). https://doi.org/10.1007/s43452-022-00501-w.

[29] Zhao, Y. Gao, Y. Wu, S. Chen, L. and Zhang, C. (2021). Experimental and numerical study of failure characteristics of brittle rocks with single internal 3D open-type flaw. Acta Geotechnica, 16(10). https://link.springer.com/article/10.1007/s11440-021-01285-8.

[30] Hou, Z. Yuan, R. Chen, Y. Sun, Wei. (2024). Crack propagation process in double-flawed granite under compression using digital image correlation method and numerical simulation. Scientific Reports, 14. http://dx.doi.org/10.1038/s41598-024-72302-5.

[31] Huang, H. S.(2022). Influence of crack location and crack number on the responses of 3D representative unit cell of unidirectional composites under tension in the fiber direction. Composite Materials. 56(20), http://dx.doi.org/10.1177/00219983221109947.

[32] Yin, F. Li, Y. Li, K. Zhang, SH. Wang, CH. Dai, F. Wang, K. (2023). Mechanical behaviors and failure mechanism of flawed sandstone containing infillings under freeze-thaw cycles and uniaxial compression. Theoretical and Applied Fracture Mechanics, 126. https://doi.org/10.1016/j.tafmec.2023.103979.

[33] Fan, X. Li, K. Lai, H. Xie, Y. Cao, R. Zheng, J. (2018). Internal stress distribution and cracking around flaws and openings of rock block under uniaxial compression: Aparticle mechanics approach. Computers and Geotechnics, 102. https://doi.org/10.1016/j.compgeo.2018.06.002.

[34] Zhao, Y. Gao, Y. Wu, S. Chen, L. and Zhang, C. (2021). Experimental and numerical study of failure characteristics of brittle rocks with single internal 3D open-type flaw. Acta Geotechnica, 16(10). https://link.springer.com/article/10.1007/s11440-021-01285-8.

[35] Shen, B. (1995). The mechanism of fracture coalescence in compression—experimental study and numerical simulation. Engineering Fracture Mechanics, 51(1). https://doi.org/10.1016/0013-7944(94)00201-R.

[36] Zhang, X. P. and Wong, L. N. Y. (2012). Cracking processes in rock-like material containing a single flaw under uniaxial compression: A numerical study based on parallel bonded-particle model approach. Rock Mechanics and Rock Engineering, 45(5). http://dx.doi.org/10.1007/s00603-011-0176-z.

[37] Zheng, L. Huang, D. Li, X. Hu, X. (2020). Numerical analysis of fracture behaviour on marble containing two flaws. Advances in Civil Engineering, 1. http://dx.doi.org/10.1155/2020/6278289.

[38] Diao, Y. Wang, W. Guo, Y. Song, J.(2025). Mesoscopic damage and failure characteristics of through-boundary type locked rock masses under confining pressure, Computational Particle Mechanics. https://doi.org/10.1007/s40571-025-01037-5

[39] Stöcklin, J. (1968). Structural history and tectonics of Iran: a review. American Association of Petroleum Geologists Bulletin, 52.

[40] Shahbazi, H. Siebel, W. Pourmoafee, M. Ghorbani, M. Sepahi, A. Shang, CK. Vousoughi, A, M. (2010). Geochemistry and U–Pb zircon geochronology of the Alvand plutonic complex in Sanandaj–Sirjan Zone (Iran): new evidence for Jurassic magmatism. Journal of Asian Earth Sciences, 39. https://doi.org/10.1016/j.jseaes.2010.04.014.

[41] Valizadeh, M. Cantagrel, J. (1975). Premières données radiométriques (K–Ar et Rb–Sr) sur les micas du complexes magmatique du Mont Alvand, Pres Hamadan (Iran occidental). Comptes Rendus de l'Academie des Sciences, Paris 281, 1083–6.

[42] Eshraghi, S. A. and Mohammadi Gharai, M. (2003). Geological Map of Tuyserkan 1/100000, Geological Survey and Mineral exploration of Iran, Tehran.

[43] Baharifar, AA. Moinevaziri, H. Bellon, H. Piqué, A. (2004). The crystal-line complexes of Hamadan (Sanandaj–

Sirjan zone, western Iran): metasedimentary Mesozoic sequences affected by Late Cretaceous tectono-metamorphic and plutonic events. Comptes Rendus Geoscience, 336. https://doi.org/10.1016/j.crte.2004.09.014.

[44] Shahbazi, H, Barjastehو H. Sepahi, A. Mottagi, T, A.(2019). Emplacement and evolution of the Alvand batholith in the shallow level of crust, Hamedan, West of Iran. Geosciences, 28. http://dx.doi.org/10.22071/gsj.2019.84267.

[45] Miri, M. Sepahi, A. Maanijou, M. Lucci, F. (2024). Rare earth element (REE) partitioning in amphibole-bearing medium grade metamorphic rocks from the Alvand Complex (Sanandaj-Sirjan Zone, NW Iran), Periodico di Mineralogia, 93. doi: 10.13133/2239-1002/18284.

[46] Huang, Y. Yang, S. Ranjith, G. Zhao, J. (2017). Strength failure behavior and crack evolution mechanism of granite containing pre-existing non- coplanar holes: experimental study and particle flow modeling, Computers and Geotechnics. 88. http://dx.doi.org/10.1016/j.compgeo.2017.03.015.

[47] Zhong, Z. Deng, R. LV, L. Fu, X. Yu, J. (2018). Fracture mechanism of naturally cracked rock around an inverted U-shaped opening in a biaxial compression test. International Journal of Rock Mechanics and Mining Sciences, 103. http://dx.doi.org/10.1016/j.ijrmms.2018.01.047.

[48] Zhou, X. Li, J. Lin, H. (2020). Analysis of internal stress distribution and mechanics characteristics of pre-existing cavity in brittle rock under triaxial cyclic loading. Frontiers in Earth Science, 8. https://doi: 10.3389/feart.2020.00033.